Atmospheric
Chemistry
and Physics
Discussions

1 **Light absorption property and potential source of particulate brown carbon in**
2 **the Pearl River Delta region of China**

3

4 Zhujie Li[1,2], Haobo Tan[2]*, Jun Zheng[1]*, Li Liu[2,3], Yiming Qin[4], Nan Wang[2], Fei Li[2], Yongjie
5 Li[5], Mingfu Cai[3], Yan Ma[1], and Chak K. Chan[4]

6

7 [1]School of Environmental Science and Engineering, Nanjing University of Information Science
8 and Technology, Nanjing, China
9 [2]Key Laboratory of Regional Numerical Weather Prediction, Institute of Tropical and Marine
10 Meteorology, China Meteorological Administration, Guangzhou, China
11 [3]Department of Atmospheric Science, Sun yat-sen University, Guangzhou, China
12 [4]School of Energy and Environment, City University of Hong Kong, Hong Kong, China
13 [5]Department of Civil and Environmental Engineering, Faculty of Science and Technology,
14 University of Macau, Macau, China

15

16 *Correspondence to: Haobo Tan (hbtan@grmc.gov.cn) and Jun Zheng (zheng.jun@nuist.edu.cn)*

17

Atmospheric
Chemistry
and Physics
Discussions

Open Access

18   **Abstract:**

19   Brown carbon (BrC) is a type of light-absorbing component of organic aerosol (OA), covering

20   from near-ultraviolet (UV) to visible wavelength ranges, and thus may cause additional aerosol

21   radiative effect in the atmosphere. While high concentrations of OA have been observed in the

22   Pearl River Delta (PRD) region of China, optical properties and the corresponding radiative

23   forcing of BrC in PRD are still not well understood. In this work, we conducted a set of

24   comprehensive measurements of atmospheric particulate matters from 29 November 2014 to 5

25   January 2015 to investigate aerosol composition, optical properties, source origins and radiative

26   forcing effects at a suburban station of Guangzhou. Particle absorption Ångström exponent

27   (AAE) was deduced and utilized to differentiate light absorption by BrC from black carbon

28   (BC). The results showed that the average absorption contributions of BrC were 25.9±9.0% at

29   370 nm, 19.7±7.9% at 470 nm, 14.1±6.9% at 520nm, 11.6±5.6% at 590nm and 7.7±4.4% at

30   660nm, respectively. A sensitivity analysis of the evaluation of absorption Ångström exponent

31   of BC (AAE_{BC}) was conducted based on the Mie theory calculation, assuming that the BC-

32   containing aerosol was internally mixed, with a core-shell configuration. The corresponding

33   uncertainty of BrC absorption contribution was acquired. We found that variations in the

34   imaginary refractive index (RI) of BC core can significantly affect the estimation of BrC

35   absorption contribution. However, BrC absorption contribution was relatively less sensitive to

36   the real part of RI of BC core and was least sensitive to the real part of RI of non-light absorbing

37   shell. BrC absorption was closely related to aerosol potassium cation content (K^+), a common

38   tracer of biomass burning emission, which was most likely associated with straw burning in the

39   rural area of western PRD. Diurnal variation of BrC absorption revealed that primary organic

40   aerosol had a larger BrC absorption capacity than secondary organic aerosol (SOA) had.

41   Radiative transfer simulations showed that BrC absorption may cause 2.2±2.3 W m^{-2} radiative

42   forcing at the top of atmosphere (TOA) and contribute 14.2±6.2% of the aerosol warming effect.

43   A chart was constructed to conveniently assess the BrC radiative forcing efficiency in the

44   studied area with reference to a certain aerosol single-scattering albedo (*SSA*) and BrC

45   absorption contribution at various wavelengths. Evidently, BrC radiative forcing efficiency was

46   higher in shorter wavelength.

1 Introduction

BC and organic carbon (OC) are the dominant carbonaceous aerosol components, which are

mainly originated from anthropogenic activities and have attracted great environmental

concerns in the rapidly developing regions. Carbonaceous aerosols can not only exert adverse

impacts on public health like other particulate matters, but also significantly affect terrestrial

radiation balance with enormous uncertainties. In previous studies, BC was often considered to

be the only light-absorbing species (Andreae and Gelencser, 2006) and OC was believed to be

only able to scatter light, i.e., causing the cooling effect (Bond et al., 2011). Nevertheless, it has

been reported that some fraction of organic aerosols (OA) may also specifically contribute to

light absorption from near-UV to visible wavelength range and is termed as brown carbon (BrC)

(Kirchstetter et al., 2004). BrC optical properties are strongly affected by its chemical

compositions and physical structures, which are related to different BrC sources. BrC could

originate not only from direct emissions, including smoldering biomass burning or any type of

incomplete fuel combustion process (Cheng et al., 2011; T. C. Bond et al., 1999), but also from

secondary organic aerosol formation process, such as aqueous phase reactions in acidic

solutions (Desyaterik et al., 2013) or volatile organic compounds (VOC) oxidation (Laskin et

al., 2015; Sareen et al., 2010). In addition, BrC could possess complicated molecular

composition and intermix with other substances, such as BC, non-absorbing OA and other

inorganic materials, making it complicated to investigate BrC optical properties.

BC absorption is commonly assumed to be wavelength-independent. However, light absorption

property of BrC is believed to be wavelength-dependent, which can be represented by distinct

absorption Ångström exponent (AAE) values, i.e., the power exponent of light absorption

coefficient. A typical threshold AAE of BC (AAE_{BC}) of 1.6 has been recommend to distinguish

BrC from BC (Lack and Cappa, 2010) and the AAE of BrC has been reported with a wider

range (2 to 7) (Hoffer et al., 2005). Based on the difference in wavelength dependence of light

absorption between BC and BrC, previous studies have applied the AAE method to segregate

light absorption by BrC through multi-wavelength optical measuring apparatus, such as 3-

74   wavelength Photoacoustic Soot Spectrometer (PASS-3) (Lack and Langridge, 2013), multi-

75   wavelength Aethalometer (Olson et al., 2015), and so on. Based on the AAE method, BrC

76   absorption contribution has been estimated to be about 6 to 41 % of total aerosol light

77   absorption at short wavelengths, for instance, at 370 nm and 405 nm (Washenfelder et al., 2015).

78   Unity AAE_{BC} is commonly used from the ~300 nm up to ~700 nm (Moosmüller et al., 2011)

79   when evaluating BrC absorption contribution using the AAE method. However, it has been

80   reported that AAE_{BC} can be influenced by the mixing state, BC core size and morphology (Lack

81   and Cappa, 2010). The lensing effect of the coating shell may enhance BC light absorption, the

82   magnitude of which may also depend on wavelength and can alter the value of AAE_{BC} (Liu et

83   al., 2018). Moreover, different values of AAE_{BC} have been found in the NIR and UV ranges

84   (Wang et al., 2018). Therefore, using the default $AAE_{BC} = 1$ may lead to uncertainty in BrC

85   absorption coefficient estimation.

86   Quantifying BrC optical absorption accurately is essential to interpret aerosol optical depth

87   (AOD) and the corresponding aerosol direct radiative forcing (DRF) on the atmosphere can

88   also be evaluated, if the *SSA* and extinction coefficient of aerosols are known. The estimation

89   of the DRF of BrC showed a distinct seasonal variation, indicating the influence from different

90   absorption properties of BrC (Arola et al., 2015). A global simulation study indicated that the

91   averaged warming effect at the TOA caused by the BrC absorption can be up to 0.11 W m^{-2},

92   corresponding to ~25% of that predicted from BC absorption only (Feng et al., 2013).

93   During the last three decades, rapid economic development has led to severe air pollution

94   problems in the PRD region (Chan and Yao, 2008). With rapid increases in automobile

95   population and factories, high loadings of SOA have often been observed (Tan et al., 2016).

96   Biofuel usage may also play a significant role during the wintertime air pollution events in PRD,

97   indicating that the contribution from BrC light absorption cannot be ignored (Wu et al., 2018).

98   Recently, BrC light absorption has been quantified by Qin et al. (2018) using the AAE method

99   in the PRD region. OA chemical composition was simultaneously measured by a high

100   resolution time-of-flight aerosol mass spectrometer and it was found that organic aerosol

101   originated from biomass burning possessed the most intense absorption capability and was

102   largely responsible for the BrC absorption. Qin et al. (2018) also suggested that correlations

103   between OA chemical compositions and BrC absorption were wavelength-dependent.

Atmospheric
Chemistry
and Physics
Discussions

104 In this paper, we have applied the homologous AAE segregation method to quantify the fraction

105 of aerosol light absorption by BrC using measurements of a seven-wavelengths aethalometer.

106 The potential error incurred with this methodology has been determined using Mie theory

107 simulations, especially for various complex refractive indexes of BC core and the coating

108 material. The correlation between BrC light absorption and water-soluble ions, used as the

109 source tracer, were employed to identify the potential BrC sources. An atmospheric radiative

110 transfer model also has been applied to evaluate BrC's impact on direct radiative forcing using

111 surface-based aerosol optical properties and satellite-based surface-albedo data. The

112 magnitudes of aerosol radiative forcing at the top of the atmosphere due to BC and BrC were

113 also separately quantified.

114 **2 Methodology**

115 **2.1 Sampling site**

116 Field observation was conducted at the Panyu station (23°00.2360′N, 113°21.2920′E), which

117 was one of the monitor sites of the Chinese Meteorological Administration (CMA)

118 Atmospheric Watch Network (CAWNET) located on the summit of the Dazhengang Mountain

119 (about 150 m above sea level) in Guangzhou, China. Fig. 1 shows the location of the Panyu site,

120 which is situated at the center of PRD and is separated from the residential areas by at least 500

121 m. Some agricultural fields can be found to the west of the site. Although there were no

122 significant pollution sources nearby, this suburban site was strongly affected by the pollutants

123 transported from the urban area of Guangzhou and crop residual fires from the rural area of

124 PRD. Field campaign was conducted from 29 November 2014 to 5 January 2015. During the

125 measurement period, aerosol light scattering and extinction, BC concentration, particle number

126 size distribution (PNSD), OC concentration, along with water-soluble ions concentration of

127 $PM_{2.5}$ were continuously monitored.

128 **2.2 Measurements and data analysis**

129 All instruments were housed inside the 2nd floor measurement room of a ~5-m tall, 2-story building.

130 Ambient sample was pulled in through the roof by a 2-m long, 12.7-mm OD stainless steel inlet and

131 a $PM_{2.5}$ cyclone was also used. The metal tubing was thermally insulated and maintained at a

132 constant temperature of ~25℃. A diffusion drier was also used in-line to dry the sample air relative

133 humidity (RH) below 30% before further analyses.

Atmospheric
Chemistry
and Physics
Discussions

2.2.1 Measurements of relevant species

A TSI-3936 scanning mobility particle sizer (SMPS) and a TSI-3321 aerodynamic particle sizer (APS) were utilized for the measurement of PNSD of 10 to 500 nm in mobility diameter and 0.5 to 2.5 μm in aerodynamic diameter, respectively. The aerodynamic diameters of APS data was converted into mobility diameter using a material density of 1.7 g cm^{-3}. The detailed data merging method has been described by Cheng et al. (2006). Furthermore, the pipe diffusion loss of SMPS has been corrected using the empirical formula proposed by Kulkarni et al. (1996).

An AE-33 aethalometer (Magee Scientific Inc.) was utilized for BC mass concentration measurement, which was derived from the optical attenuation using a mass absorption cross section (MAC) of 7.77 m^2 g^{-1} at 880 nm. The sensitivity of the AE-33 was about 0.03 μg m^{-3} for a 1-min time resolution and a 5.0 liters per minute (LPM) sample flow rate.

Water-soluble ions (potassium (K^+), calcium (Ca^{2+}), magnesium (Mg^{2+}), chloride (Cl^-), sulfate (SO_4^{2-}), nitrate (NO_3^-), and ammonium (NH_4^+)) were measured with a Monitor for AeRosols and Gases in Air (MARGA) (Model ADI2080, Metrohm Inc.), an on-line analyzer for semi-continuous measurements of gases and water-soluble ions in aerosols (Li et al., 2010). The MARGA was automatically calibrated with internal standard solutions during the field measurement. The MARGA utilized its own PM$_{2.5}$ sampling system provided by the manufacturer.

OC mass concentration was measured by a Sunset online EC/OC analyzer (Model RT-4) with a laser transmittance-based charring correction (Wu et al., 2018). The sample flow rate of the EC/OC analyzer was maintained at 8 LPM. For each measurement cycle of one hour, samples were collected onto a quartz filter within the first 45 min and then was thermal-optically analyzed during the remaining 15 min. Firstly, OC was completely volatized in oxygen-free helium with a stepwise ramped temperature (600 ℃ and 840 ℃). In the second stage, the temperature was reduced to 550 ℃, and then EC and pyrolyzed carbon (PC) were combusted in an oxidizing atmosphere (10% oxygen in helium), while the temperature was increased up to 870 ℃ step by step. The CO$_2$ converted from all the carbon components was then quantified by a nondispersive infrared absorption CO$_2$ sensor (Lin et al., 2009). Internal calibration peak made by 5% methane in helium was applied to quantified OC and EC. In order to correct the PC converted from OC to EC, a tunable pulsed diode laser beam was used to monitor the laser

164   transmittance through the quartz filter during the OC measurement stage (Bauer et al., 2012).

165   **2.2.2 Measurements of optical properties**

166   Light extinction by aerosols at 532 nm was detected using a cavity ring-down aerosol extinction

167   spectrometer (CRDS) (Model XG-1000, Hexin Inc.) by measuring the decay times of laser

168   intensity through the aerosol-containing sample and the filtered background air sample under

169   the same condition. The extinction coefficient (σ_{ext}) was calculated using the procedure

170   described by Khalizov et al. (2009).

171   Aerosol total scattering (σ_{sp}) was measured by a TSI-3563 integrating nephelometer at three

172   wavelengths (i.e., 450 nm, 550 nm, and 700 nm), which was calibrated with CO_2 following the

173   manual instruction. Particle free air was used to check the nephelometer background signal

174   once every two hours. The scattering coefficients at other wavelengths were extrapolated using

175   the following equations:

$$SAE = -\frac{ln\left(\sigma_{scat,\lambda_0}\right) - ln\left(\sigma_{scat,550nm}\right)}{ln(\lambda_0) - ln(550)} \quad (1)$$

176

$$\sigma_{scat}(\lambda) = \sigma_{scat}(550) \cdot \left(\frac{\lambda}{550}\right)^{-SAE} \quad (2)$$

177

178   where λ_0=450 nm for wavelengths less than 550 nm and λ_0=700 nm for wavelengths more than

179   550 nm.

180   The aethalometer was also used for multi-wavelengths light absorption measurements in this

181   study. The seven-wavelengths aerosol light attenuation coefficients (σ_{ATN}) were converted into

182   the aerosol light absorption coefficients (σ_{abs}) using Eq. (3) (Coen et al., 2010), where k is the

183   parameter to account for the loading effect, ATN is the light attenuation through the filter with

184   sample loading and C_{ref} is a fixed multiple scattering parameter.

$$\sigma_{abs} = \frac{\sigma_{ATN}}{(1 - k \cdot ATN) \cdot C_{ref}} \quad (3)$$

185

186   Real-time k value was retrieved using the dual-spot loading correction algorithm developed by

187   Drinovec et al. (2015). The detailed formula of ATN can also be found in Drinovec et al. (2015).

188   C_{ref} is considered a constant that strongly depends on the filter matrix effect. However, some

189   studies have suggested that C_{ref} may vary with wavelength (Arnott et al., 2005; Segura et al., 2014).

190   C_{ref} at 370 nm was expected to be about 12% and 18% less than C_{ref} at 532 nm for aerosol

191   component mainly from internal combustion engines and biomass burning, respectively

192   (Schmid et al., 2006). Different ambient observations also showed that C_{ref} may have regional

193   specificity, even though they were all retrieved by the same methodology (Coen et al., 2010).

194   In this study, C_{ref}=3.29 was used in Eq. (3) at each wavelength and this value was derived from

195   the slope of σ_{ATN} measured by the aethalometer vs. σ_{abs}, deduced from the CRDS and

196   nephelometer measurements. This C_{ref} was also very similar to the C_{ref} of 3.48 determined from

197   an inter-comparison study between a aethalometer and a photo-acoustic soot spectrometer

198   during a filed campaign conducted in the PRD region in 2004 (Wu et al., 2009).

199   The BC light absorption at certain wavelength was derived from the absorption coefficients σ_{abs}

200   according to the Beer-Lambert's Law and its variation between different pair of wavelengths

201   (i.e., $\sigma_{abs,BC,\lambda}$) is denoted by the Absorption Ångström exponent (AAE) equation developed by

202   Ångström (1929):

203   $$\sigma_{abs,BC,\lambda_1} = \sigma_{abs,BC,\lambda_2} \times (\lambda_1 / \lambda_2)^{-AAE_{BC}} \qquad (4)$$

204   It has been suggested that the AAE of BC may vary between short- and long-wavelength ranges

205   (Lack and Cappa, 2010) and hence applying a wavelength-independent AAE_{BC} may lead to

206   uncertainties in BC absorption calculation from one wavelength to another. In this work, the

207   light absorptions of BC at various wavelengths were retrieved by a modified wavelength-

208   dependent AAE segregation method:

209   $$\sigma_{abs,BC,\lambda_{i+1}} = \sigma_{abs,\lambda_1} \times \left(\frac{\lambda_1}{\lambda_2}\right)^{AAE_{BC,\,\lambda_1-\lambda_2}} \times \cdots \cdots \times \left(\frac{\lambda_i}{\lambda_{i+1}}\right)^{AAE_{BC,\,\lambda_i-\lambda_{i+1}}}, \; 1 < i \leq 5 \qquad (5)$$

210   Here $\sigma_{abs,BC,\lambda_i}$ (i=1, 2, 3, 4, 5, and 6) stands for the absorption coefficient due to BC alone at

211   λ_i=880, 660, 590, 520, 470 and 370 nm, respectively. $AAE_{BC,\,\lambda_i-\lambda_{i+1}}$ represents the AAE of BC

212   between a longer and a shorter wavelength and was calculated as:

213   $$AAE_{BC,\lambda_i-\lambda_{i+1}} = -\frac{ln(\sigma_{abs,BC,\lambda_i}) - ln(\sigma_{abs,BC,\lambda_{i+1}})}{ln(\lambda_i) - ln(\lambda_{i+1})} \qquad (6)$$

214   Accordingly, BrC absorption at a certain wavelength λ ($\sigma_{abs,BrC,\lambda}$) was the value of the total

215   aerosol absorption ($\sigma_{abs,\lambda}$) subtracting BC absorption ($\sigma_{abs,BC,\lambda}$):

216   $$\sigma_{abs,BrC,\lambda} = \sigma_{abs,\lambda} - \sigma_{abs,BC,\lambda} \qquad (7)$$

217   The data of light absorption at 880 nm ($\sigma_{abs,BC,880}$) was selected to represent BC absorption,

218   which shall not be affected by BrC (Drinovec et al., 2015). It has been reported that dust-related

219   contribution of $PM_{2.5}$ was normally less than 5% in wintertime Guangzhou, therefore the

220   influence from dust could be negligible in this study (Huang et al., 2014).

221   **2.2.3 Estimation of AAE_{BC}**

222   Traditionally, AAE_{BC} was believed to be close to 1.0 (Bodhaine, 1995), which has been

223   commonly used for BC measurements (Olson et al., 2015). However, studies have

224   demonstrated that AAE_{BC} can be affected by the refractive index of coating materials, mixing

225   state, morphology, and BC core size (Liu et al., 2015). Moreover, different values of AAE_{BC}

226   have been found in the NIR and UV ranges (Wang et al., 2018). Therefore, using the default

227    $AAE_{BC} = 1$ may lead to uncertainty in BrC absorption estimation. In order to obtain the correct

228   AAE_{BC}, a series of Mie theory calculations were conducted using a simplified core-shell model

229   (Bohren and Huffman, 1983; Wang et al., 2018). We used a modified BHCOAT code to

230   calculate aerosol optical properties of core-shell mixture at different wavelengths (Cheng et al.,

231   2006). In the Mie theory, a particle was taken as a perfect homogeneous sphere and its

232   extinction and scattering efficiencies, $Q_{ext,Mie,\lambda}$ and $Q_{scat,Mie,\lambda}$ are expressed as (Mie, 1908;

233   Seinfeld and Pandis, 1998):

$$Q_{ext,Mie,\lambda} = \frac{2}{\alpha^2}\sum_{n=1}^{\infty}[(2n+1)Re(a_n+b_n)] \tag{8}$$

$$Q_{scat,Mie,\lambda} = \frac{2}{\alpha^2}\sum_{n=1}^{\infty}[(2n+1)(|a_n|^2+|b_n|^2)] \tag{9}$$

236   where $\alpha = \pi D_p/\lambda$ is the size parameter; a_n and b_n are functions of the complex RI and α

237   in the Riccati-Bessel form. Re in Eq. (8) denotes that only the real part of RI is taken. The

238   absorption efficiency ($Q_{abs,Mie,\lambda}$) was thus the difference between extinction and scattering

239   efficiencies:

$$Q_{abs,Mie,\lambda} = Q_{ext,Mie,\lambda} - Q_{scat,Mie,\lambda} \tag{10}$$

241   Then the absorption coefficient $\sigma_{abs,Mie,\lambda}$ was obtained following (Bricaud and Morel, 1986):

$$\sigma_{abs,Mie,\lambda} = \int Q_{abs,Mie,\lambda} \cdot (\frac{\pi}{4}D_p^2) \cdot N(\log D_p) \cdot d\log D_p \tag{11}$$

243   where $N(\log D_p)$ is the PNSD. A two-component parameterization of dry particles, i.e., the

244   BC core and the non (or less) light-absorbing species, was applied to calculate aerosol optical

245   properties here (Wex et al., 2002). The PNSD of BC core was calculated as:

$$N(logD_p)_{core} = N(logD_p)_{measure} \cdot f_{BC} \tag{12}$$

247   where, $N(logD_p)_{measure}$ is the measured PNSD ; $(N(logD_p)_{core})$ is the BC core PNSD; f_{BC} is the

248   BC's volume fraction of total particles and is calculated as:

249
$$f_{BC} = \frac{M_{BC}}{\rho_{BC} \cdot \sum_{D_P} N(logD_p)_{measure} \cdot (\frac{\pi}{6} \cdot D_p^3)} \qquad (13)$$

250 where, ρ_{BC} is the density of BC and is assumed to be 1.5 g cm^{-3} (Ma et al., 2012); M_{BC} is the BC

251 mass concentration derived from the MAAP, which was obtained by an empirical formula from

252 Aethalometer measured BC concentration ($M_{BC,AE}$) proposed by Wu et al. (2009):

253
$$M_{BC} = 0.897 \cdot M_{BC,AE} - 0.062 \qquad (14)$$

254 The diameter of the BC core was calculated as:

255
$$D_{core} = D_p \cdot (f_{BC})^{\frac{1}{3}} \qquad (15)$$

256 The $\sigma_{abs,BC,Mie,\lambda_i}$ of all six wavelengths were calculated through the Mie model, and then the

257 AAE$_{BC}$ of these five wavelengths were obtained using Eq. (6).

258 **2.2.4 Atmospheric radiative transfer model**

259 In this work, Santa Barbara DISORT Atmospheric Radiative Transfer (SBDART) model was

260 employed to estimate the DRF of BrC absorption, i.e., its effects on the downward and upward

261 fluxes (F in W m^{-2}) of solar radiations at TOA. SBDART is a software tool that can be used to

262 compute plane-parallel radiative transfer under both clear and cloudy conditions within the

263 atmosphere. More details about this model have been described by Ricchiazzi et al. (1998).

264 Both ground measurements and remote sensing data were used in the simulation. The surface

265 albedo was derived from 500 m resolution MODIS BRDF/Albedo Model Parameters product

266 (MCD43A3, daily). The MCD43A3 products are the total shortwave broadband black-sky

267 albedo (α_{BSA}) and white-sky albedo (α_{WSA}), while the actual surface albedo (α) was computed

268 from a linear combination of α_{WSA} and α_{BSA}, weighted by the diffuse ratio (r_d) and direct ratio

269 ($1-r_d$), respectively:

270
$$\alpha = (1 - r_d) \cdot \alpha_{BSA} + r_d \cdot \alpha_{WSA} \qquad (16)$$

271 r_d was obtained from an exponential fit of Eq. (17) based on empirical observations (Roesch,

272 2004; Stokes and Schwartz, 1994):

273
$$r_d = 0.122 + 0.85e^{-4.8\mu_0} \qquad (17)$$

274 where μ_0 is the cosine of the zenith angle, calculated by the model for any specified date, time,

275 and the latitude and longitude of the site. The surface-based aerosol optical properties, including

276 aerosol light absorption coefficients of both BC and BrC, i.e., segregated from each other under

277 the assumption of unity AAE$_{BC}$, along with nephelometer measured aerosol scattering

278   coefficients, were used to calculate the *SSA* at different wavelengths according to Eq. (18),

279
$$SSA(\lambda) = \frac{\sigma_{scat,\,\lambda}}{\sigma_{abs,\,BrC,\lambda} + \sigma_{abs,\,BC,\lambda} + \sigma_{scat,\lambda}}$$
(18)

280   which was then used in the model calculation. Finally, the AOD and asymmetry factor (ASY)

281   at 440, 675 and 870 nm were derived from the Aerosol Robotic Network (AERONET)

282   measurements at the Hong Kong Polytechnic University site (Holben et al., 1998), which is

283   about 115 km to the southeast of Panyu site. The tropical atmospheric profile was used in the

284   SBDART model based on the prevailing weather conditions in PRD. The aerosol DRF (ΔF)

285   was calculated as the difference between downward and upward radiation flux:

286
$$\Delta F = F\downarrow - F\uparrow$$
(19)

287   **3 Results and discussion**

288   **3.1 Aerosol light absorption and uncertainty of BC and BrC optical segregation**

289   When the AAE_{BC} was assumed to be unity, the campaign-averaged σ_{BrC} were respectively

290   18.0±14.1 Mm^{-1} at 370 nm, 10.0±8.5 Mm^{-1} at 470 nm, 6.0±5.5 Mm^{-1} at 520 nm, 4.2±3.7 Mm^{-1}

291   at 590 nm, and 2.3±2.2 Mm^{-1} at 660 nm. At the corresponding wavelengths, BrC absorption

292   contributed 25.9±9.0%, 19.7±7.9%, 14.1±6.9%, 11.6±5.6%, and 7.7±4.4% to the total aerosol

293   absorption (see Fig. 2). Evidently, aerosol light absorption was predominantly due to BC,

294   however BrC also played a significant part, especially at shorter wavelengths. Table 1 shows

295   the inter-comparison of BrC light absorption in the near UV rang between this work and other

296   studies in the East Asia region. Clearly, the reported values range substantially and our result is

297   toward the lower value end.

298   In reality AAE_{BC} may vary significantly with the BC containing aerosol of different size, mixing

299   state, and morphology (Lack and Langridge, 2013; Scarnato et al., 2013). In fact, some studies

300   showed that AAE of large size pure BC core may be less than 1.0 (Liu et al., 2018), and that

301   AAE of BC coated with non-absorbing shell may be larger than unity (Lack and Cappa, 2010).

302   Theoretically, the magnitude of BC absorptions can be apparently affected by both parts of the

303   complex refractive indexes (RI) and thus AAE_{BC} may also vary with RIs of both the BC core

304   and coating shell. In fact, RI was also one of the least known properties of BC and other coating

305   materials of negligibly absorbing capability. So far reported refractive index of BC core ($\tilde{m}_{core}$)

306   displays a wide range of variations (Liu et al., 2018). Typically, the real and imaginary parts of

Atmospheric
Chemistry
and Physics
Discussions

307   RI can vary from 1.5 to 2.0 and 0.5 to 1.1, respectively. In addition, the shell was assumed to

308   be consisting of non-absorbing material, i.e., its imaginary RI was set to be close to zero (10^{-7}).

309   The real part of the shell RI may vary from 1.35 to 1.6 due to the presence of OA (Redmond

310   and Thompson, 2011; Zhang et al., 2018) and inorganic salts (Erlick et al., 2011). Hence, it is

311   necessary to investigate the uncertainties associated with the variations in AAE_{BC} and the

312   corresponding BrC absorption contribution estimations by varying the RIs of both the BC core

313   and the non-absorbing shell. Based on the core-shell configuration, a suite of Mie theory

314   computation was performed for AAE_{BC} with specific wavelength-independent complex

315   refractive indexes (RI = $a - bi$). The results are presented in Table 2. Generally, for wavelengths

316   toward the UV range, AAE_{BC} deviated negatively from unity and the shorter the wavelength

317   was the more was the deviation. For wavelengths toward the NIR range, the trend of AAE_{BC}

318   was just reversed. It is also clearly shown that for all wavelength ranges, AAE_{BC} increased with

319   increasing real RI of the BC core but anti-correlated with the imaginary RI of the BC core. For

320   the extreme cases (Model run 19 and 20 in Table 2), the corresponding averaged BrC absorption

321   contribution can be as high as 42.7±7.0% and as low as 14.3±11.4% at 370 nm. Therefore, the

322   estimation of BrC absorption contribution can be significantly affected by the choice of AAE_{BC}.

323   However, for the cases typically encountered in the atmosphere, especially in the 500 to 600

324   nm range, AAE_{BC} was very close to one.

325   Figure 3 shows the impacts of RI on the evaluations of AAE_{BC} and BrC absorption contribution,

326   where the RI of BC core was set constant, i.e., $\widetilde{m}_{core}$=1.80 - 0.54i and the real part of shell's RI

327   varied from 1.35 to 1.6 at an interval of 0.05, with the imaginary part of shell's RI set at 10^{-7}.

328   As shown in Fig 3a, the calculated AAE_{BC} was higher than 1.0 at longer wavelength and lower

329   than 1.0 at shorter wavelength (the red line in Fig. 3 denotes AAE_{BC}=1). Even the shell material

330   was assumed non-absorbing, variation in the real RI of the shell still led to changes of shell's

331   refractivity and correspondingly altered its lensing effect, causing the fluctuation in calculated

332   AAE_{BC} values between 520 and 660 nm. In other wavelength intervals, the AAE_{BC} increased

333   with increasing real part of shell's RI. In Fig. 3b, under the same conditions as in Fig. 3a,

334   average BrC absorption contributed 23.7% ~ 27.4% at 370 nm, 13.1% ~ 17.7% at 470 nm, 7.4%

335   ~ 11.0% at 520 nm, 4.8% ~ 8.2% at 590 nm, and -0.1% ~ 4.2% at 660 nm to the total aerosol

336   absorption, respectively. Interestingly, the magnitude of BrC absorption contribution not only

Atmospheric
Chemistry
and Physics
Discussions

337   decreased with increasing wavelength, but also decreased with increasing real RI of the shell at

338   certain wavelength, which was most likely due to the absorption enhancement of BC core

339   caused by the increased leasing effects of the coating material.

340   The impacts of BC core on AAE_{BC} and BrC absorption contribution are shown in Fig. 4, where

341   the shell was assumed as non-absorbing (RI=1.55 - $10^{-7}i$) and the RIs were wavelength-

342   independent. The left panels (Figs. 4a and 4b) were obtained by fixing the imaginary RI of BC

343   core to 0.54 but varying the real RIs from 1.6 to 2.0 with a step of 0.1; the right panels (Figs.

344   4c and 4d) were done with a constant real RI of BC cores (1.8) but a varying imaginary RI from

345   0.6 to 1.0 with an incremental of 0.1. As shown in Figs. 4a and 4c, the AAE_{BC} at a certain

346   wavelength generally increased with increasing real RIs (Fig. 4a) but decreased with increasing

347   imaginary RI (Fig 4c). The AAE_{BC} appeared to be more sensitive to the imaginary RI than the

348   real RI of BC core, for the fact that the imaginary RI was directly related to light-absorbing

349   properties of particles. In Fig. 4b, within the specified real RI (1.6 to 2.0) of BC core, BrC on

350   average contributed 20.4% ~ 28.7% at 370 nm, 10.1% ~ 18.1% at 470 nm, 4.4% ~ 11.8% at

351   520 nm, 2.0% ~ 8.2% at 590 nm, and -2.0% ~ 3.3% at 660 nm to the total aerosol absorption,

352   respectively. Similarly, in Fig. 4d, within these specific BC core's imaginary RI (0.4 to 1.0),

353   BrC on average contributed 19.9% ~ 37.0 % at 370 nm, 10.7% ~ 24.1% at 470 nm, 5.3% ~

354   16.7% at 520 nm, 3.2 % ~ 11.8 % at 590 nm, and 0.01 % ~ 5.6 % at 660 nm to the total aerosol

355   absorption, respectively.

356   Figure 4 demonstrated that the variation of the imaginary RI of BC core will cause the most

357   significant impact on the estimated BrC absorption contributions, indicating that the

358   morphology and structure of BC emitted from different sources will lead to a large uncertainty

359   in BrC estimation. At the same time, the influence arisen from varying real RI of BC core was

360   relatively moderate. Nevertheless, Fig. 3 demonstrated that alteration of the real RI of the non-

361   absorbing shell caused the least impact than that caused by the variations of the complex RI of

362   BC core. Please note that $\sigma_{abs,BrC}$ was extrapolated with an assumed unity AAE_{BC}, which was

363   among a reasonable range at 370 nm but may be significantly overestimated within other longer

364   wavelengths according to Mie theory calculation results. Moreover, many studies demonstrated

365   that BrC showed a stronger light absorbance in the UV-visible wavelength range, where data at

366   370 nm were often chosen to represent BrC light absorption under the assumption of a

Atmospheric
Chemistry
and Physics
Discussions

367 wavelength-independent unity AAE$_{BC}$ (Andreae and Gelencser, 2006; Olson et al., 2015). In

368 both Fig. 3 and Fig. 4, negative BrC absorption contributions were obtained at longer

369 wavelengths, which were due to the uncertainties associated with the calculation and the

370 dominance (near 100%) of BC absorption at these wavelengths.

371 We want to point out that most BC containing particles are often observed as fractal rather than

372 spherical in shape (Katrinak et al., 1993). Since the core-shell Mie model is under the

373 assumption that all particles are spherical, it may lead to potential uncertainty for the estimation

374 of AAE$_{BC}$ and BrC absorption contributions. Moreover, during a closure study in the PRD

375 region Tan et al. (2016) have found that the actual BC mixing state was partially core-shell and

376 partially external mixing. During a test run with the assumption of external mixing, we found

377 that BrC contribution would become significantly higher.

378 **3.2 Characteristics of BrC light absorption, water-soluble ion and OC concentration**

379 Globally, BrC have been observed to be highly correlated with biomass and biofuel burning

380 emissions (Laskin et al., 2015). Since large quantity of sylvite is present in biomass burning

381 particles, K$^+$ abundancy has often been used as a biomass burning tracer (Levine, 1991). Figure

382 5 presents the time series of OC mass concentration, K$^+$ concentration, and BrC absorption from

383 29 November 2014 to 5 January 2015 at the Panyu site. The range of OC concentration obtained

384 from the OC/EC online analyzer was from 1.5 to 67.6 μg cm^{-3} and the campaign average was

385 12.1 ± 7.8 μg cm^{-3}. The BrC absorption hourly mean data was between 0.2 and 70.8 Mm^{-1} and

386 the campaign average was 17.6 ± 12.4 Mm^{-1}. On the other hand, average K$^+$ concentration was

387 1.0 ± 0.7 μg cm^{-3} (ranging from 0 to 5.4 μg cm^{-3}). Clearly, similar trends among OC, K$^+$, and

388 BrC absorption can be seen during this field campaign (Fig. 5).

389 In order to investigate the origins of these observed OC, K$^+$, and BrC. Wind rose plots (as shown

390 in Fig. 6) were generated for OC, K$^+$, and BrC absorption, respectively. All three panels of Fig.

391 6 show consistently that the three substances were associated with the same wind pattern. For

392 the whole campaign period, the highest values of OC, K$^+$, and $\sigma_{abs,BrC,370nm}$ were mostly

393 associated with southwesterly winds of relatively low wind speed (~2 m s^{-1}). The relatively

394 higher OC and K$^+$ concentrations were highly related to the seasonal straw burning in the

395 countryside of PRD located to the west of the Panyu station. On the contrary, OC and K$^+$

396 concentrations during periods with easterly winds were substantially lower than those during

Atmospheric
Chemistry
and Physics
Discussions

397 westerly winds. The wind rose plot of $\sigma_{abs,BrC,370nm}$ is shown in Fig. 6c. Similar to OC and K$^+$,

398 $\sigma_{abs,BrC,370nm}$ showed higher values in the weak (<2 m s^{-1}) westerly wind and lower values from

399 the north and south, indicating that BrC absorption was likely attributed to local sources and

400 was accumulated under calm wind conditions. However, there was detectable difference among

401 the three rose plots in the maximum concentration direction. The possible explanation was that

402 although biomass burning emission was believed to be the dominant primary source of OC, K$^+$,

403 and BrC, their emission ratios were highly variable and may change with the types of biofuel,

404 burning conditions, and may even vary during different stages of burning (Burling et al., 2012).

405 Although biomass burning emissions contain substantial light-absorbing BrC, further

406 atmospheric aging process may significantly reduce its light-absorbing capability (Satish et al.,

407 2017). Moreover, secondary formation may also lead to BrC formation inside these primary

408 aerosols, such as humic-like substances formed through aqueous-phase reactions have been

409 suggested to be an important component of BrC (Andreae and Gelencser, 2006).

410 To further explore possible sources of BrC optical absorption, the diurnal variations of OC, K$^+$,

411 $\sigma_{abs,BrC,370nm}$, and $\sigma_{abs,BrC,370nm}$ /OC values are plotted in Fig. 7. Diurnal variation of OC at the

412 Panyu site appeared to be dominated by the development of planetary boundary layer (PBL)

413 height, i.e., primary emissions were accumulating at night and were swiftly diluted by vertical

414 mixing in the morning. The slight increase of OC in the afternoon indicated that photochemistry

415 may still contribute weakly to the SOA formation. Figure 7b shows the diurnal variation of K$^+$.

416 Unlike OC, K$^+$ shows a distinct peak around 6 AM, which was consistent with the breakfast

417 time and was most likely due to cooking activities using biofuel. It is still a common practice

418 to collect straw as biofuel in the local rural area, which can be visually spotted. The diurnal

419 profile of $\sigma_{abs,BrC,370nm}$ (see Fig. 7c) shows the combined feature of OC and K$^+$, since both

420 primary and secondary processes will affect its intensity. The nighttime rising trend was most

421 likely attributed to straw burning activities in early winter in nearby rural area that continued

422 to accumulate within the shallow PBL (Jiang et al., 2013). $\sigma_{abs,BrC,370nm}$/OC, i.e., the mass

423 absorption coefficient of BrC (MAC$_{BrC}$) (Fig. 7d), shows a relatively flat pattern with a

424 pronounced dip in the afternoon and higher values at nighttime, which was likely due to the

425 enhanced primary emissions and stable stratification at nighttime. The declining trends during

426 the late morning and afternoon hours indicated that aging process and photochemical

Atmospheric
Chemistry
and Physics
Discussions

427   production may reduce BrC's light-absorbing capacity (Qin et al., 2018).

428   Furthermore, Fig. 8 shows the linear regression analysis results to evaluate the correlations

429   between $\sigma_{abs,BrC,370nm}$ and OC, K^+, Ca^{2+}, Mg^{2+}, Cl^-, SO_4^{2-}, NO_3^-, NH_4^+ concentrations,

430   respectively. The best correlations can be found between $\sigma_{abs,BrC,370nm}$ and K^+ and OC

431   (R^2=0.4889 and 0.4872, respectively), followed by NO_3^- (R^2=0.3267) and NH_4^+ (R^2=0.3234).

432   Both nitrogen oxides (NO_x) and ammonia (NH_3) can be found in biomass burning plumes

433   (Andreae and Merlet, 2001). Nitrate can be converted from NO_x through atmospheric reactions

434   and NO_x may originate from many combustion processes, such as biomass burning or any kind

435   of fossil fuel usage (Elliott et al., 2009). Source apportionment analysis of OA and BrC

436   absorption in Beijing and Guangzhou illustrated that biomass burning organic aerosol (BBOA)

437   correlated well with BrC light absorption (Qin et al., 2018; Xie et al., 2018). Thus, the

438   significant correlation between BrC absorption and NO_3^-/NH_4^+ reaffirmed that biomass burning

439   was the crucial emission source of BrC observed in this work. Although the geographic location

440   of observation site was situated in a coastal area and K^+ also could be found in sea salt (Pio et

441   al., 2008), it should be noted that the prevailing wind direction during winter was from the north

442   (see Fig. 3), which will drive marine air parcels away from the site. High concentrations of Ca^{2+}

443   and Mg^{2+} are often found in dust-related aerosols (Lee et al., 1999). $\sigma_{abs,BrC,370nm}$ showed poor

444   correlations with both Ca^{2+} and Mg^{2+}, indicating that dust-related aerosol components

445   contribute insignificantly to the total aerosol mass loading and thus dust may not affect the AAE

446   segregation method used in this work. Although sulfur dioxide (SO_2) may also be emitted by

447   biomass burning, SO_4^{2-} is often believed to be secondary in nature and the presents of other

448   intense SO_2 sources (e.g., automobile and industrial emissions) will further smear the

449   correlation between BrC and SO_4^{2-}. Sources of Cl^- include both combustions and sea salt spray

450   (Waldman et al., 1991). Although the prevailing wintertime wind direction was from the north,

451   sea salt still can be carried to the site by weak sea breeze and thus Cl^- may not show considerable

452   correlation with BrC.

453   **3.3 BrC radiative forcing efficiency**

454   The radiative effects of aerosol scattering, BrC absorption, and BC absorption were investigated

455   by the SBDART model. For each investigated variable under cloud-free condition, we run the

456   model twice to calculate the DRF at TOA with and without the investigated variable.

Atmospheric
Chemistry
and Physics
Discussions

457   Accordingly, the difference of ΔF between the two simulations was considered as the radiative

458   effect of the investigated variable. The results showed that the average radiative forcing at TOA

459   by scattering, BrC absorption, and BC absorption were respectively -21.0±5.5 W m^{-2}, 2.2±2.3

460   W m^{-2}, and 11.3±5.0 W m^{-2}. Furthermore, BrC absorption was attributed to 14.2±6.2% of the

461   warming effect caused by aerosol light-absorption, demonstrating that the nonnegligible role of

462   BrC in radiative forcing evaluation.

463   We also calculated the BrC radiative forcing efficiency (RFE) under various SSA (ranging from

464   0.7 to 0.99) at three wavelengths, i.e., 440 nm, 675 nm, and 870 nm. The RFE was denoted as

465   the radiative forcing normalized by the AOD. The average AOD and ASY at the three

466   wavelengths were respectively 0.370 and 0.697 at 440 nm, 0.214 and 0.635 at 675 nm, and

467   0.153 and 0.618 at 870 nm. A solar zenith angle of 55° and an average shortwave broadband

468   surface albedo (0.119) were used in the calculation. The results were plotted as a set of lookup

469   charts of RFE as a function of the surface BrC absorption contribution (see Fig. 9).

470   In general, for any wavelength RFE increased with increasing BrC absorption contribution for

471   a certain SSA, indicating BrC was a more efficient radiative forcing agent due to BrC's

472   preferential absorbance in shorter wavelength range. However, for a certain BrC absorption

473   contribution RFE increased with decreasing SSA, i.e., higher portion of light-absorbing aerosol

474   components can lead to more efficient radiative forcing. The trend among panels (a), (b), and

475   (c) in Fig. 9 demonstrated that the effect of BrC absorption contribution on REF was

476   wavelength-dependent, i.e., BrC was a weaker radiative forcing agent at longer wavelength,

477   which is also consistent with BrC's wavelength-dependent light-absorbing property. The black

478   stars in Fig. 9 denote the average SSA and BrC absorption contribution conditions during this

479   campaign, i.e., 0.025 W m^{-2} per unit AOD at 440 nm (Fig. 9a), 0.007 W m^{-2} per unit AOD at

480   675 nm (Fig. 9b), and 0.0002 W m^{-2} per unit AOD at 870 nm (Fig. 9c). These results suggested

481   that the average value of REF decreased distinctly from 440 nm to 870 nm, not only because

482   of the lower BrC absorption contribution, but also due to BrC REF's wavelength-dependence.

483   It also should be noted that the simulations were based on SSA measured under dry conditions.

484   Under the typical ambient conditions of PRD, the SSA might be markedly enhanced by aerosol

485   water uptake (Jung et al., 2009), and then, the BrC radiative forcing efficiency might be less.

486   Moreover, Fig. 9 is also served as a lookup table to conveniently assess the BrC radiative

Atmospheric
Chemistry
and Physics
Discussions

487   forcing efficiency at different wavelengths with different BrC absorption contribution for a

488   certain *SSA*.

4 Conclusion

490   In this work, light absorption due to BrC in the PRD region of China was quantitatively deduced

491   during the winter season of 2014. The average BrC light absorption contribution ranged from

492   7.7±4.4% at 660 nm up to 25.9±9.0% at 370 nm, when AAE_{BC} was set to unity. The uncertainty

493   in BrC absorption estimation associated with this assumption was further investigated. Using

494   the absorption coefficients of BC calculated according to the Mie theory and the observed total

495   aerosol absorption coefficients, we have estimated the AAE_{BC} and hence the BrC absorption

496   contribution for different core-shell RI configuration. The results showed that at 370 nm

497   variations of shell's real RI (1.35 to 1.6) may decrease BrC absorption contribution from 27.4%

498   to 23.7%; variations of core's real RI (1.6 to 2.0) may reduce BrC absorption contribution from

499   28.7% to 20.4%.; variations of core's imaginary RI (0.4 to 1.0) can cause BrC absorption

500   contribution to increase from 19.9% to 37.0%. These results indicated that the optical properties

501   of the BC core and shell material can significantly affect the accuracy of BrC absorption

502   contribution estimations.

503   Additionally, measurements of major water-soluble inorganic ions (including K^+, NO_3^-, and

504   NH_4^+) and particulate OC showed consistent features with $\sigma_{abs,BrC,370nm}$, implying that the BrC

505   was associated with the biomass-burning emissions from nearby rural area. Moreover, the

506   diurnal trend of $\sigma_{abs,BrC,370nm}$/OC indicated that primary biomass burning emissions can produce

507   intense light-absorbing BrC, while the photochemical aging process may weaken BrC's light-

508   absorbing capability.

509   Using a radiative transfer model (i.e., SBDART), we estimated the BrC effects on aerosol's

510   radiative forcing. The average shortwave aerosol direct radiative forcing due to scattering, BrC

511   absorption, and BC absorption at TOA were evaluated to be -21.0±5.5 W m^{-2}, 2.2±2.3 W m^{-2},

512   and 11.3±5.0 W m^{-2}, respectively. BrC absorption accounted for 14.2±6.2% of the total

513   shortwave solar absorption warming effect at TOA, indicating that BrC might be an important

514   climate forcing agent, which was largely neglected in current climate models. To facilitate the

515   estimation of climate effects of BrC, a set of look-up charts were constructed for the

516   investigated area based on the default tropical atmosphere profile, averaged surface albedo,

517   averaged asymmetry factor, and surface-measured aerosol properties (BrC absorption

518   contribution, *SSA*, and AOD). Therefore, the role of BrC radiative forcing efficiency at three

519   wavelengths can be conveniently assessed for certain *SSA* and BrC absorption contribution.

520

521   *Author contributions*

522   HT, JZ, YM, and CC designed the experiments and ZL, LL, YQ, NW, FL, YL, and MC carried

523   out the field measurements and the data analysis. ZL and YQ performed Mie theory simulation.

524   ZL, JZ, and HT prepared the manuscript with comments from all co-authors.

525

531

Atmospheric
Chemistry
and Physics
Discussions

References:

Andreae, M. O., and Merlet, P.: Emission of trace gases and aerosols from biomass burning, Global Biogeochem. Cycles, 15, 955-966, 2001.

Andreae, M. O., and Gelencser, A.: Black carbon or brown carbon? The nature of light-absorbing carbonaceous aerosols, Atmospheric Chemistry & Physics, 6, 3131-3148, 2006.

Ångström, A.: On the Atmospheric Transmission of Sun Radiation and on Dust in the Air, Geografiska Annaler, 11, 156-166, 1929.

Arnott, W. P., Hamasha, K., Moosmüller, H., Sheridan, P. J., and Ogren, J. A.: Towards Aerosol Light-Absorption Measurements with a 7-Wavelength Aethalometer: Evaluation with a Photoacoustic Instrument and 3-Wavelength Nephelometer, Aerosol Science and Technology, 39, 17-29, 10.1080/027868290901972, 2005.

Arola, A., Schuster, G. L., Pitkänen, M. R. A., Dubovik, O., Kokkola, H., Lindfors, A. V., Mielonen, T., Raatikainen, T., Romakkaniemi, S., Tripathi, S. N., and Lihavainen, H.: Direct radiative effect by brown carbon over the Indo-Gangetic Plain, Atmospheric Chemistry and Physics, 15, 12731-12740, 10.5194/acp-15-12731-2015, 2015.

Bauer, J. J., Yu, X.-Y., Cary, R., Laulainen, N., and Berkowitz, C.: Characterization of the Sunset Semi-Continuous Carbon Aerosol Analyzer, Journal of the Air & Waste Management Association, 59, 826-833, 10.3155/1047-3289.59.7.826, 2012.

Bodhaine, B. A.: Aerosol absorption measurements at Barrow, Mauna Loa and the south pole, Journal of Geophysical Research Atmospheres, 100, 8967–8975, 1995.

Bohren, C. F., and Huffman, D. R.: Wiley: Absorption and Scattering of Light by Small Particles - Craig F. Bohren, Donald R. Huffman, Optics & Laser Technology, 31, 328-328, 1983.

Bond, T. C., Zarzycki, C., Flanner, M. G., and Koch, D. M.: Quantifying immediate radiative forcing by black carbon and organic matter with the Specific Forcing Pulse, Atmospheric Chemistry and Physics, 11, 1505-1525, 10.5194/acp-11-1505-2011, 2011.

Bricaud, A., and Morel, A.: Light attenuation and scattering by phytoplanktonic cells: a theoretical modeling, Appl. Opt., 25, 571-580, 10.1364/AO.25.000571, 1986.

Burling, I. R., Yokelson, R. J., Akagi, S. K., Urbanski, S. P., Wold, C. E., Griffith, D. W. T., Johnson, T. J., Reardon, J., and Weise, D. R.: Airborne and ground-based measurements of the trace gases and particles emitted by prescribed fires in the United States (vol 11, pg 12197, 2011), Atmospheric Chemistry and Physics, 12, 103-103, 10.5194/acp-12-103-2012, 2012.

Chan, C. K., and Yao, X.: Air pollution in mega cities in China, Atmospheric Environment, 42, 1-42, http://dx.doi.org/10.1016/j.atmosenv.2007.09.003, 2008.

Cheng, Y., He, K. B., Zheng, M., Duan, F. K., Du, Z. Y., Ma, Y. L., Tan, J. H., Yang, F. M., Liu, J. M., Zhang, X. L., Weber, R. J., Bergin, M. H., and Russell, A. G.: Mass absorption efficiency

567   of elemental carbon and water-soluble organic carbon in Beijing, China, Atmospheric
568   Chemistry and Physics, 11, 11497-11510, 10.5194/acp-11-11497-2011, 2011.

569   Cheng, Y. F., Eichler, H., Wiedensohler, A., Heintzenberg, J., Zhang, Y. H., Hu, M., Herrmann,
570   H., Zeng, L. M., Liu, S., Gnauk, T., Brüggemann, E., and He, L. Y.: Mixing state of elemental
571   carbon and non-light-absorbing aerosol components derived from in situ particle optical
572   properties at Xinken in Pearl River Delta of China, Journal of Geophysical Research:
573   Atmospheres, 111, doi:10.1029/2005JD006929, 2006.

574   Coen, M. C., Weingartner, E., Apituley, A., Ceburnis, D., Fierzschmidhauser, R., Flentje, H.,
575   Henzing, J. S., Jennings, S. G., Moerman, M., and Petzold, A.: Minimizing light absorption
576   measurement artifacts of the Aethalometer: evaluation of five correction algorithms,
577   Atmospheric Measurement Techniques, 3, 457-474, 2010.

578   Desyaterik, Y., Sun, Y., Shen, X., Lee, T., Wang, X., Wang, T., and Collett, J. L.: Speciation of
579   "brown" carbon in cloud water impacted by agricultural biomass burning in eastern China,
580   Journal of Geophysical Research: Atmospheres, 118, 7389-7399, 10.1002/jgrd.50561, 2013.

581   Drinovec, L., Močnik, G., Zotter, P., Prévôt, A. S. H., Ruckstuhl, C., Coz, E., Rupakheti, M.,
582   Sciare, J., Müller, T., Wiedensohler, A., and Hansen, A. D. A.: The "dual-spot" Aethalometer:
583   an improved measurement of aerosol black carbon with real-time loading compensation,
584   Atmospheric Measurement Techniques, 8, 1965-1979, 10.5194/amt-8-1965-2015, 2015.

585   Elliott, E. M., Kendall, C., Boyer, E. W., Burns, D. A., Lear, G. G., Golden, H. E., Harlin, K.,
586   Bytnerowicz, A., Butler, T. J., and Glatz, R.: Dual nitrate isotopes in dry deposition: Utility for
587   partitioning NOxsource contributions to landscape nitrogen deposition, Journal of Geophysical
588   Research, 114, 10.1029/2008jg000889, 2009.

589   Erlick, C., Abbatt, J. P. D., and Rudich, Y.: How Different Calculations of the Refractive Index
590   Affect Estimates of the Radiative Forcing Efficiency of Ammonium Sulfate Aerosols, Journal
591   of the Atmospheric Sciences, 68, 1845-1852, 10.1175/2011jas3721.1, 2011.

592   Feng, Y., Ramanathan, V., and Kotamarthi, V. R.: Brown carbon: a significant atmospheric
593   absorber of solar radiation?, Atmospheric Chemistry and Physics, 13, 8607-8621, 10.5194/acp-
594   13-8607-2013, 2013.

595   Hoffer, A., Gelencsér, A., Guyon, P., and Kiss, G.: Optical properties of humic-like substances
596   (HULIS) in biomass-burning aerosols, Atmospheric Chemistry & Physics, 5, 3563-3570, 2005.

597   Holben, B. N., Eck, T. F., Slutsker, I., Tanré, D., Buis, J. P., Setzer, A., Vermote, E., Reagan, J.
598   A., Kaufman, Y. J., and Nakajima, T.: AERONET—A Federated Instrument Network and Data
599   Archive for Aerosol Characterization, Remote Sensing of Environment, 66, 1-16, 1998.

600   Huang, R.-J., Zhang, Y., Bozzetti, C., Ho, K.-F., Cao, J.-J., Han, Y., Daellenbach, K. R., Slowik,
601   J. G., Platt, S. M., Canonaco, F., Zotter, P., Wolf, R., Pieber, S. M., Bruns, E. A., Crippa, M.,
602   Ciarelli, G., Piazzalunga, A., Schwikowski, M., Abbaszade, G., Schnelle-Kreis, J.,
603   Zimmermann, R., An, Z., Szidat, S., Baltensperger, U., Haddad, I. E., and Prévôt, A. S. H.:

604   High secondary aerosol contribution to particulate pollution during haze events in China,
605   Nature, 514, 218-222, 10.1038/nature13774, 2014.

606   Jiang, D., Wang, C., Wu, D., Deng, X., Huang, X., Tan, H., Li, F., and Deng, T.: Diurnal
607   variation of atmospheric boundary layer over Wushan station, Guangzhou using wind profiler
608   radar (in Chinese), Journal of Tropical Meteorology, 29, 129-135, 2013.

609   Jung, J., Lee, H., Kim, Y. J., Liu, X., Zhang, Y., Gu, J., and Fan, S.: Aerosol chemistry and the
610   effect of aerosol water content on visibility impairment and radiative forcing in Guangzhou
611   during the 2006 Pearl River Delta campaign, Journal of Environmental Management, 90, 3231-
612   3244, http://dx.doi.org/10.1016/j.jenvman.2009.04.021, 2009.

613   Katrinak, K. A., Rez, P., Perkes, P. R., and Buseck, P. R.: Fractal geometry of carbonaceous
614   aggregates from an urban aerosol, Environmental Science & Technology, 27, págs. 225-238,
615   1993.

616   Khalizov, A. F., Xue, H., Wang, L., Zheng, J., and Zhang, R.: Enhanced light absorption and
617   scattering by carbon soot aerosol internally mixed with sulfuric acid, The journal of physical
618   chemistry. A, 113, 1066-1074, 10.1021/jp807531n, 2009.

619   Kirchstetter, T. W., Novakov, T., and Hobbs, P. V.: Evidence that the spectral dependence of
620   light absorption by aerosols is affected by organic carbon, Journal of Geophysical Research:
621   Atmospheres, 109, n/a-n/a, 10.1029/2004jd004999, 2004.

622   Kulkarni, P., Baron, P. A., and Willeke, K.: Aerosol measurement : principles, techniques, and
623   applications, Van Nostrand Reinhold, 807-808 pp., 1996.

624   Lack, D. A., and Cappa, C. D.: Impact of brown and clear carbon on light absorption
625   enhancement, single scatter albedo and absorption wavelength dependence of black carbon,
626   Atmospheric Chemistry and Physics, 10, 4207-4220, 10.5194/acp-10-4207-2010, 2010.

627   Lack, D. A., and Langridge, J. M.: On the attribution of black and brown carbon light absorption
628   using the Ångström exponent, Atmospheric Chemistry and Physics, 13, 10535-10543,
629   10.5194/acp-13-10535-2013, 2013.

630   Laskin, A., Laskin, J., and Nizkorodov, S. A.: Chemistry of atmospheric brown carbon,
631   Chemical reviews, 115, 4335-4382, 10.1021/cr5006167, 2015.

632   Lee, E., Chan, C. K., and Paatero, P.: Application of positive matrix factorization in source
633   apportionment of particulate pollutants in Hong Kong, Atmospheric Environment, 33, 3201-
634   3212, https://doi.org/10.1016/S1352-2310(99)00113-2, 1999.

635   Levine, J.: Biomass Burning Aerosols in a Savanna Region of the Ivory Coast, French Forum,
636   235-236, 1991.

637   Li, H., Han, Z., Cheng, T., Du, H., Kong, L., Chen, J., Zhang, R., and Wang, W.: Agricultural
638   Fire Impacts on the Air Quality of Shanghai during Summer Harvesttime, Aerosol and Air

Atmospheric
Chemistry
and Physics
Discussions

639   Quality Research, 10.4209/aaqr.2009.08.0049, 2010.

640   Lin, P., Hu, M., Deng, Z., Slanina, J., Han, S., Kondo, Y., Takegawa, N., Miyazaki, Y., Zhao,
641   Y., and Sugimoto, N.: Seasonal and diurnal variations of organic carbon in PM2.5in Beijing
642   and the estimation of secondary organic carbon, Journal of Geophysical Research, 114,
643   10.1029/2008jd010902, 2009.

644   Liu, C., Chung, C. E., Yin, Y., and Schnaiter, M.: The absorption Ångström exponent of black
645   carbon: from numerical aspects, Atmospheric Chemistry and Physics, 18, 6259-6273,
646   10.5194/acp-18-6259-2018, 2018.

647   Liu, D., Taylor, J. W., Young, D. E., Flynn, M. J., Coe, H., and Allan, J. D.: The effect of
648   complex black carbon microphysics on the determination of the optical properties of brown
649   carbon, Geophysical Research Letters, 42, 613-619, 2015.

650   Ma, N., Zhao, C. S., Müller, T., Cheng, Y. F., Liu, P. F., Deng, Z. Z., Xu, W. Y., Ran, L., Nekat,
651   B., van Pinxteren, D., Gnauk, T., Müller, K., Herrmann, H., Yan, P., Zhou, X. J., and
652   Wiedensohler, A.: A new method to determine the mixing state of light absorbing carbonaceous
653   using the measured aerosol optical properties and number size distributions, Atmos. Chem.
654   Phys., 12, 2381-2397, 10.5194/acp-12-2381-2012, 2012.

655   Mie, G.: Beitrage Zur Optik Truber Medien, Speziell Kolloidaler Metalosungen, Annalen Der
656   Physik, 25, 377, 1908.

657   Moosmüller, H., Chakrabarty, R. K., Ehlers, K. M., and Arnott, W. P.: Absorption Ångström
658   coefficient, brown carbon, and aerosols: basic concepts, bulk matter, and spherical particles,
659   Atmospheric Chemistry and Physics, 11, 1217-1225, 10.5194/acp-11-1217-2011, 2011.

660   Nakayama, T., Ikeda, Y., Sawada, Y., Setoguchi, Y., Ogawa, S., Kawana, K., Mochida, M.,
661   Ikemori, F., Matsumoto, K., and Matsumi, Y.: Properties of light‐absorbing aerosols in the
662   Nagoya urban area, Japan, in August 2011 and January 2012: Contributions of brown carbon
663   and lensing effect, Journal of Geophysical Research Atmospheres, 119, 12,721-712,739, 2015.

664   Olson, M. R., Victoria Garcia, M., Robinson, M. A., Van Rooy, P., Dietenberger, M. A., Bergin,
665   M., and Schauer, J. J.: Investigation of black and brown carbon multiple-wavelength-dependent
666   light absorption from biomass and fossil fuel combustion source emissions, Journal of
667   Geophysical Research: Atmospheres, 120, 6682-6697, 10.1002/2014jd022970, 2015.

668   Pio, C. A., Legrand, M., Alves, C. A., Oliveira, T., Afonso, J., Caseiro, A., Puxbaum, H.,
669   Sanchez-Ochoa, A., and Gelencsér, A.: Chemical composition of atmospheric aerosols during
670   the 2003 summer intense forest fire period, Atmospheric Environment, 42, 7530-7543, 2008.

671   Qin, Y. M., Tan, H. B., Li, Y. J., Li, Z. J., Schurman, M. I., Liu, L., Wu, C., and Chan, C. K.:
672   Chemical characteristics of brown carbon in atmospheric particles at a suburban site near
673   Guangzhou, China, Atmospheric Chemistry and Physics Discussions, 1-23, 10.5194/acp-2018-
674   730, 2018.

Atmospheric
Chemistry
and Physics
Discussions

675   Redmond, H., and Thompson, J. E.: Evaluation of a quantitative structure-property relationship
676   (QSPR) for predicting mid-visible refractive index of secondary organic aerosol (SOA),
677   Physical chemistry chemical physics : PCCP, 13, 6872-6882, 10.1039/c0cp02270e, 2011.

678   Ricchiazzi, P., Yang, S., Gautier, C., and Sowle, D.: SBDART: A Research and Teaching
679   Software Tool for Plane-Parallel Radiative Transfer in the Earth's Atmosphere, Bulletin of the
680   American   Meteorological   Society,   79,   2101-2114,   10.1175/1520-
681   0477(1998)079<2101:Sarats>2.0.Co;2, 1998.

682   Roesch, A.: Use of Moderate-Resolution Imaging Spectroradiometer bidirectional reflectance
683   distribution function products to enhance simulated surface albedos, Journal of Geophysical
684   Research, 109, 10.1029/2004jd004552, 2004.

685   Sareen, N., Schwier, A. N., Shapiro, E. L., Mitroo, D., and McNeill, V. F.: Secondary organic
686   material formed by methylglyoxal in aqueous aerosol mimics, Atmospheric Chemistry and
687   Physics, 10, 997-1016, 10.5194/acp-10-997-2010, 2010.

688   Satish, R., Shamjad, P., Thamban, N., Tripathi, S., and Rastogi, N.: Temporal Characteristics of
689   Brown Carbon over the Central Indo-Gangetic Plain, Environmental science & technology, 51,
690   6765-6772, 10.1021/acs.est.7b00734, 2017.

691   Scarnato, B. V., Nielsen, K., Vahidinia, S., and Richard, D.: Effect of Aggregation and Mixing
692   on optical properties of Black Carbon, 2013,

693   Schmid, O., Artaxo, P., Arnott, W. P., Chand, D., Gatti, L. V., Frank, G. P., Hoffer, A., Schnaiter,
694   M., and Andreae, M. O.: Spectral light absorption by ambient aerosols influenced by biomass
695   burning in the Amazon Basin. I: Comparison and field calibration of absorption measurement
696   techniques, Atmos. Chem. Phys., 6, 3443-3462, 10.5194/acp-6-3443-2006, 2006.

697   Segura, S., Estellés, V., Titos, G., Lyamani, H., Utrillas, M. P., Zotter, P., Prévôt, A. S. H.,
698   Močnik, G., Alados-Arboledas, L., and Martínez-Lozano, J. A.: Determination and analysis of
699   in situ spectral aerosol optical properties by a multi-instrumental approach, Atmospheric
700   Measurement Techniques, 7, 2373-2387, 10.5194/amt-7-2373-2014, 2014.

701   Seinfeld, J. H., and Pandis, S. N.: Atmospheric Chemistry and Physics, John Wiley & Sons, Inc,
702   New York, 1998.

703   Stokes, G. M., and Schwartz, S. E.: The Atmospheric Radiation Measurement (ARM) Program:
704   Programmatic Background and Design of the Cloud and Radiation Test Bed, Bulletin of the
705   American Meteorological Society, 75, 1201–1221, 1994.

706   T. C. Bond, †, M. Bussemer, B. Wehner, S. Keller, R. J. Charlson, a., and Heintzenberg‡, J.:
707   Light Absorption by Primary Particle Emissions from a Lignite Burning Plant, Environmental
708   Science & Technology, 33, 3887-3891, 1999.

709   Tan, H., Yin, Y., Li, F., Liu, X., Chan, P. W., Deng, T., Deng, X., Wan, Q., and Wu, D.:
710   Measurements of particle number size distributions and new particle formations events during

711   winter in the Pearl River Delta region, China, Journal of Tropical Meteorology, 22, 191-199,
712   10.16555/j.1006-8775.2016.02.009, 2016.

713   Waldman, J. M., Lioy, P. J., Zelenka, M., Jing, L., Lin, Y. N., He, Q. C., Qian, Z. M., Chapman,
714   R., and Wilson, W. E.: Wintertime measurements of aerosol acidity and trace elements in
715   Wuhan, a city in central China, Atmospheric Environment. Part B. Urban Atmosphere, 25, 113-
716   120, https://doi.org/10.1016/0957-1272(91)90045-G, 1991.

717   Wang, J., Nie, W., Cheng, Y., Shen, Y., Chi, X., Wang, J., Huang, X., Xie, Y., Sun, P., Xu, Z.,
718   Qi, X., Su, H., and Ding, A.: Light absorption of brown carbon in eastern China based on 3-
719   year multi-wavelength aerosol optical property observations and an improved absorption
720   Ångström exponent segregation method, Atmospheric Chemistry and Physics, 18, 9061-9074,
721   10.5194/acp-18-9061-2018, 2018.

722   Washenfelder, R. A., Attwood, A. R., Brock, C. A., Guo, H., Xu, L., Weber, R. J., Ng, N. L.,
723   Allen, H. M., Ayres, B. R., and Baumann, K.: Biomass burning dominates brown carbon
724   absorption in the rural southeastern United States, Geophysical Research Letters, 42, 653-664,
725   2015.

726   Wex, H., Neusüß, C., Wendisch, M., Stratmann, F., Koziar, C., Keil, A., Wiedensohler, A., and
727   Ebert, M.: Particle scattering, backscattering, and absorption coefficients: An in situ closure
728   and sensitivity study, Journal of Geophysical Research Atmospheres, 107, LAC-1-LAC 4-18,
729   2002.

730   Wu, C., Wu, D., and Yu, J. Z.: Quantifying black carbon light absorption enhancement with
731   a novel statistical approach, Atmospheric Chemistry and Physics, 18, 289-309, 10.5194/acp-
732   18-289-2018, 2018.

733   Wu, D., Mao, J., Deng, X., Tie, X., Zhang, Y., Zeng, L., Li, F., Tan, H., Bi, X., Huang, X., Chen,
734   J., and Deng, T.: Black carbon aerosols and their radiative properties in the Pearl River Delta
735   region, Science in China Series D: Earth Sciences, 52, 1152-1163, 10.1007/s11430-009-0115-
736   y, 2009.

737   Xie, C., Xu, W., Wang, J., Wang, Q., Liu, D., Tang, G., Chen, P., Du, W., Zhao, J., Zhang, Y.,
738   Zhou, W., Han, T., Bian, Q., Li, J., Fu, P., Wang, Z., Ge, X., Allan, J., Coe, H., and Sun, Y.:
739   Vertical characterization of aerosol optical properties and brown carbon in winter in urban
740   Beijing, China, Atmospheric Chemistry and Physics Discussions, 1-28, 10.5194/acp-2018-788,
741   2018.

742   Yuan, J. F., Huang, X. F., Cao, L. M., Cui, J., Zhu, Q., Huang, C. N., Lan, Z. J., and He, L. Y.:
743   Light absorption of brown carbon aerosol in the PRD region of China, Atmospheric Chemistry
744   and Physics, 16, 1433-1443, 10.5194/acp-16-1433-2016, 2016.

745   Zhang, Y., Li, Z., Sun, Y., Lv, Y., and Xie, Y.: Estimation of atmospheric columnar organic
746   matter (OM) mass concentration from remote sensing measurements of aerosol spectral
747   refractive indices, Atmospheric Environment, 179, 107-117, 10.1016/j.atmosenv.2018.02.010,

748   2018.

749

750

751   **Table 1.** Observational studies of the BrC light absorption coefficient and contribution in near

752   ultraviolet wavelength range in East Asia.

| Periods	Location	λ (nm)	Mean BrC absorption coefficient	Mean BrC absorption contribution	Instrumentation	Reference
Nov.2014 – Jan.2015	Guangzhou (China)	370	18.3 Mm^{-1}	25.9 %	Aethalometer AE-33	This study
Jan.2014 – Feb.2014; Sep.2014 – Oct.2014	Shenzhen (China)	405	3.0 Mm^{-1} 1.4 Mm^{-1}	11.7% (winter) 6.3% (fall)	PASS-3	Yuan et al. (2016)
Nov.2014	Heshan (China)	405	3.9 Mm^{-1}	12.1%	PASS-3	Yuan et al. (2016)
Nov.2016– Dec.2016	Beijing (China)	370	106.4 Mm^{-1} 93.8 Mm^{-1}	46% (at ground) 48% (at 260m)	Aethalometer AE-33	Xie et al. (2018)
Jun.2013 – May.2016	Nanjing (China)	370	35.8 Mm^{-1}	16.7%	Aethalometer AE-31	Wang et al. (2018)
Jan. 2012	Nagoya (Japan)	405	Not detected	11% (300℃) 17% (400℃)	Thermodenuder PASS-3	Nakayama et al. (2015)

753

754   **Table 2.** AAE_{BC} estimation from core-shell Mie theory model.
755

| Model Run Number | Complex Refractive index | | | | AAE_{BC} | | | | |
| | Core | | Shell | | | | | | |
	Real part	Imaginary part	Real part	Imaginary part	370-470nm	470-520nm	520-590nm	590-660nm	660-880nm
1	1.6	0.54i	1.55	10^{-7} i	0.76	0.95	0.92	1.00	1.13
2	1.7	0.54i	1.55	10^{-7} i	0.77	0.98	0.95	1.03	1.18
3	1.8	0.54i	1.55	10^{-7} i	0.79	1.01	0.98	1.06	1.22
4	1.9	0.54i	1.55	10^{-7} i	0.81	1.04	1.01	1.09	1.27
5	2	0.54i	1.55	10^{-7} i	0.83	1.07	1.04	1.11	1.32
6	1.8	0.4i	1.55	10^{-7} i	0.88	1.10	1.05	1.12	1.27
7	1.8	0.5i	1.55	10^{-7} i	0.81	1.04	1.00	1.08	1.24
8	1.8	0.6i	1.55	10^{-7} i	0.75	0.97	0.95	1.03	1.20
9	1.8	0.7i	1.55	10^{-7} i	0.70	0.92	0.90	0.99	1.16
10	1.8	0.8i	1.55	10^{-7} i	0.65	0.86	0.86	0.94	1.12
11	1.8	0.9i	1.55	10^{-7} i	0.60	0.81	0.82	0.90	1.08
12	1.8	1.0i	1.55	10^{-7} i	0.56	0.77	0.78	0.87	1.05
13	1.8	0.54i	1.35	10^{-7} i	0.81	0.90	0.99	1.09	1.10
14	1.8	0.54i	1.4	10^{-7} i	0.81	0.92	0.98	1.10	1.12
15	1.8	0.54i	1.45	10^{-7} i	0.80	0.94	0.97	1.10	1.15
16	1.8	0.54i	1.5	10^{-7} i	0.80	0.98	0.97	1.08	1.19
17	1.8	0.54i	1.55	10^{-7} i	0.79	1.01	0.98	1.06	1.22
18	1.8	0.54i	1.6	10^{-7} i	0.79	1.04	1.01	1.02	1.25
19	1.6	1.0i	1.35	10^{-7} i	0.50	0.62	0.70	0.79	0.88
20	2	0.4i	1.6	10^{-7} i	0.92	1.18	1.15	1.13	1.40

756

757
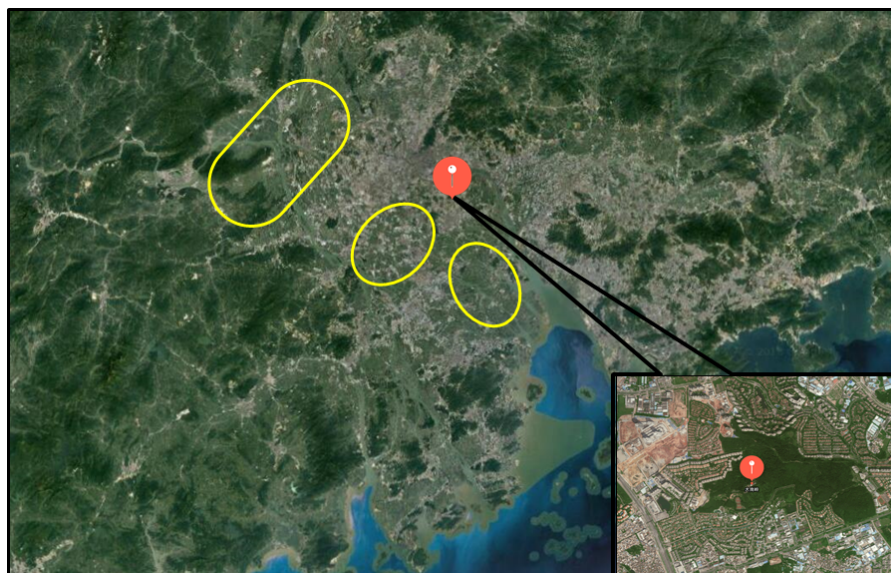
Figure 1. The location of Panyu station (CAWNET) in the PRD region (indicated by the red

dot). The plain areas within the yellow circles are the main rural areas of western PRD.

758

759

760

Atmospheric
Chemistry
and Physics
Discussions

761
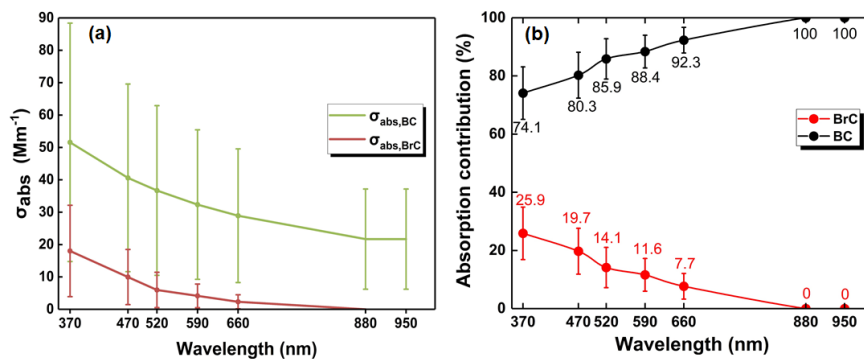
Figure 2. (a) BC and BrC particle average light absorption coefficient at different wavelengths; the whiskers represent the error bar of one standard deviation. (b) Contributions of BC and BrC to the total light absorption coefficient at different wavelengths; the whiskers represent the error bar of one standard deviation.

Atmospheric
Chemistry
and Physics
Discussions

767

768
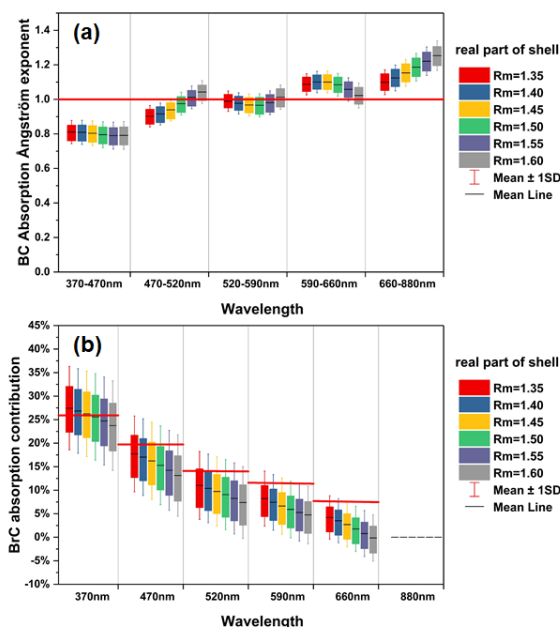
Figure 3. Influence of wavelength-independent refractive index of the non-absorbing
shell on the (a) AAEs and (b) BrC absorption contribution with a constant BC core
refractive index ($\widetilde{m}_{core}$=1.80-0.54i). The imaginary part of non-(or less-) absorbing
shell was set to 10^{-7}, while real part varied from 1.6 to 2.0. In each panel, the boundaries
of the box represented the 75th and the 25th percentiles; the whiskers above and below
each box indicate the error bar of one standard deviation; the black lines among the
boxes denote the average values. In panel a, red line indicates where AAE_{BC}=1. In panel
b, the red lines indicate the BrC absorption contribution calculated with AAE_{BC}=1 in
each wavelength.

778

779

780
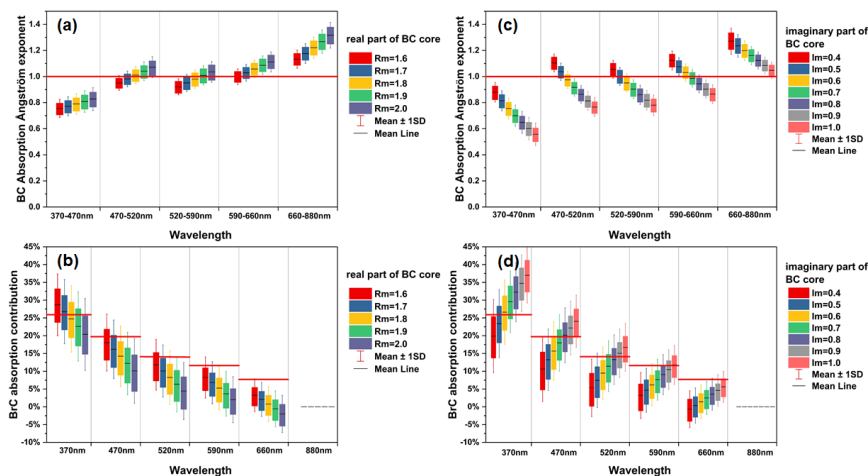
Figure 4. Influence of wavelength-independent refractive index of the BC core on the AAEs and BrC absorption with a constant shell refractive index ($\widetilde{m}_{shell}=1.55\text{-}10^{-7}i$). A fixed BC imaginary part of 0.54 was used for panels a and b, while real RI varies from 1.6 to 2.0. A fixed BC real RI of 1.8 is used for panels c and d, while imaginary part varies from 0.4 to 1.0. In each panel, the boundaries of the box represent the 75th and the 25th percentiles; the whiskers above and below each box is the error bar of one standard deviation; the black lines among the boxes indicate the average values. In panels a and b, red line indicate where $AAE_{BC}=1$. In panels c and d, the red lines indicate the BrC absorption contribution calculated with $AAE_{BC}=1$ at each wavelength.
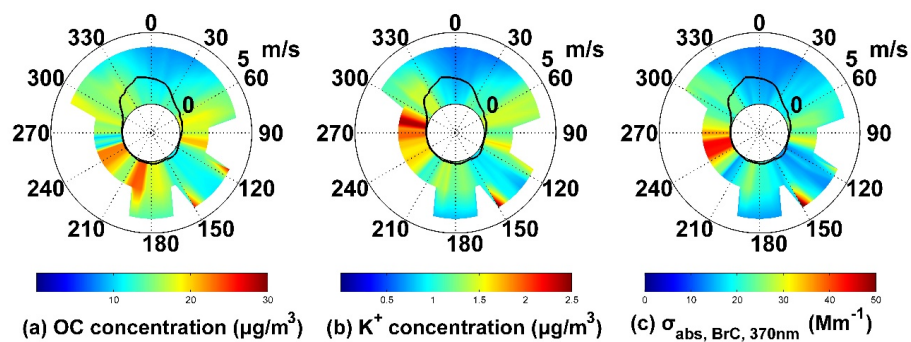
790

791
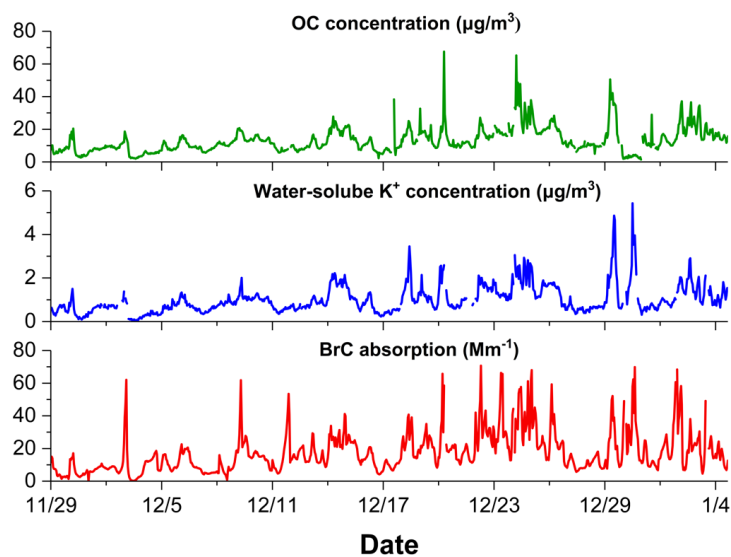
Figure 5. Time series of OC aerosol mass concentration (green line), water-soluble K^+ mass

concentration (blue line), and BrC light absorption (red line).

794

795

(a) OC concentration (µg/m³)   (b) K⁺ concentration (µg/m³)   (c) $\sigma_{abs, BrC, 370nm}$ (Mm⁻¹)

796   Figure 6. Wind rose plots of OC (a), K$^+$ (b), and $\sigma_{abs,BrC,370nm}$ (c). In each panel, the black solid

797   lines denote the frequency of wind direction. The shaded contour represents the average values

798   of corresponding species for that wind speed (radial length) and wind direction (transverse

799   direction) in the polar coordinates.

800
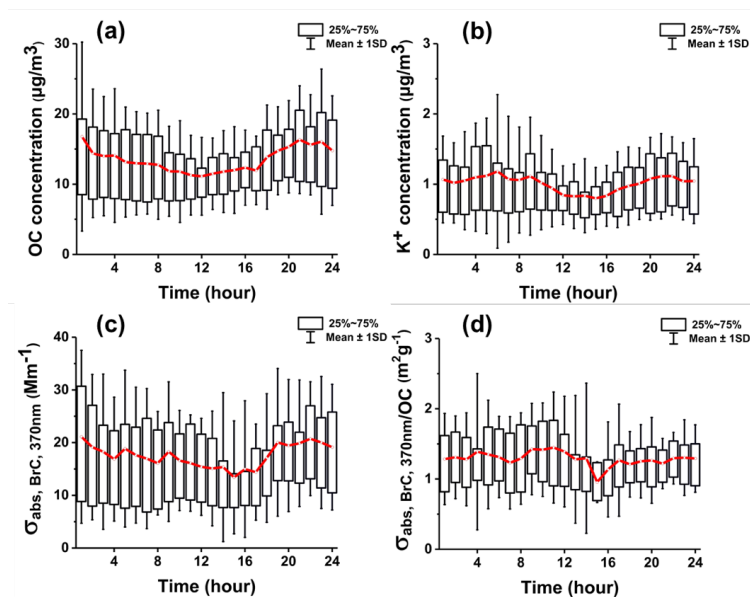
Figure 7. Box-whisker plots of diurnal trends of OC concentration (a), diurnal trends of water-soluble K+ concentration (b), diurnal trends of $\sigma_{abs,BrC,370nm}$ (c), and diurnal trends of $\sigma_{abs,BrC,370nm}$ /OC (d). Red traces represent the variation of average value. Upper and lower boundaries of the box represent the 75th and the 25th percentiles; the whiskers above and below each box represent the error bar of one standard deviation.
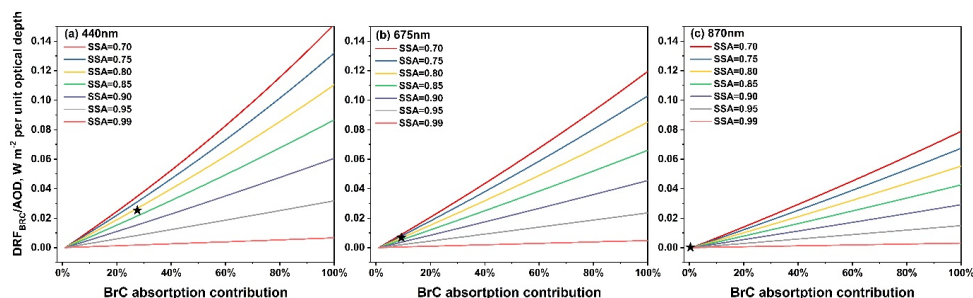
Atmospheric
Chemistry
and Physics
Discussions
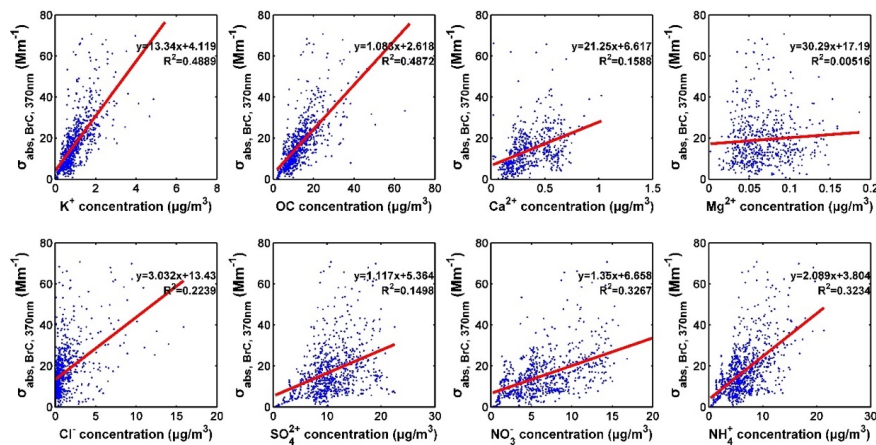
808

809   Figure 8. Correlations between the BrC absorption coefficients at 370 nm and OC, water-

810   soluble K^+, Ca^{2+}, Mg^{2+}, Cl^-, SO_4^{2-}, NO_3^-, NH_4^+ aerosol concentration.

811

Figure 9. BrC radiative forcing efficiencies, defined as the BrC TOA direct radiative forcing divided by AOD, as a function of BrC to BC absorption ratio and *SSA* measured at surface. The average AOD of the three wavelengths, the average ASY of the three wavelengths, a solar zenith angle of 55°, and the average shortwave broadband surface albedo were used in the calculation. The black star corresponds to average *SSA* and BrC absorption contribution determined from this campaign.